Diffuse optical fluorescence tomography using time-resolved data acquired in transmission

Frederic Leblond*[a], Simon Fortier[a] and Michael P. Friedlander[b]
[a]ART Advanced Research Technologies Inc., 2300 Alfred Nobel, Saint-Laurent, Quebec, Canada H4S 2A4
[b]Department of Computer Science, University of British Columbia, Vancouver, British Columbia, Canada V6K 2C6

ABSTRACT

We present an algorithm using data acquired with a time-resolved system with the goal of reconstructing sources of fluorescence emanating from the deep interior of highly scattering biological tissues. A novelty in our tomography algorithm is the integration of a light transport model adapted to rodent geometries. For small volumes, our analysis suggest that neglecting the index of refraction mismatch between diffusive and non-diffusive regions, as well as the curved nature of the boundary, can have a profound impact on fluorescent images and spectroscopic applications relying on diffusion curve fitting. Moreover, we introduce a new least-squares solver with bound constraints adapted for optical problems where a physical non-negative constraint can be imposed. Finally, we find that maximizing the time-related information content of the data in the reconstruction process significantly enhances the quality of fluorescence images. Preliminary noise propagation and detector placement optimization analysis are also presented.

Keywords: Near-infrared imaging, fluorescence, diffuse optical tomography, photon transport, diffusion approximation

1. INTRODUCTION

The place occupied by near-infrared (**NIR**) imaging within the multi-disciplinary field of molecular imaging has been growing in the last years. In particular, the existence of a niche that fluorescence NIR imaging can occupy is indisputable partly because of its intrinsic advantages (*e.g.*, low cost, non-invasive) when compared to other modalities such as positron emission tomography (**PET**), magnetic resonance imaging (**MRI**), and computed tomography (**CT**). However, several challenges remain before fluorescence NIR tomography algorithms combined with a mono-modal clinical device can provide quantitatively reliable information capitalizing on the specificity and sensitivity of fluorescent probes. The objective is to derive valuable structural, biochemical, and biophysical information on cells and tissues in a non-invasive manner.

This paper summarizes preliminary efforts aiming to develop a fluorescence imager with tomographic capabilities. The system uses a raster-scan technique in order to acquire time-resolved data in trans-illumination. As explained below, the access to time-resolved data can be important because it has the potential to help circumvent some of the basic obstacles associated with NIR imaging (*e.g.*, highly heterogeneous nature of small animals, ill-posedness of the problem). In Section 2, we present an overview of the physical model and the numerical techniques used to perform fluorescence image reconstructions. Some emphasis is put on the development of a novel algorithm allowing the treatment of surface curvature and non-trivial boundary conditions. We also introduce a new bound-constrained least-squares solver algorithm (**BCLS**). In Section 3, we present a performance evaluation of BCLS using synthetic data generated with the diffuse optical forward model described in Section 2. In Section 4, we conclude with the presentation of fluorescence images reconstructed based on experimental data acquired with a time-resolved prototype developed at ART Advanced Research Technologies Inc. (**ART**).

2. PHYSICAL MODEL

We consider fluorescence spectroscopy based on single photon emissions associated with a red-shifted transition from an excited electronic state to a lower state. The so-called Stokes shift between the peak of the absorption band and that of the fluorescence band is a measure of the relaxation process associated with non-radiative transitions occurring in the excited state. The relevant intrinsic physical properties of fluorescent molecules are the absorption cross-section (σ), the lifetime (τ) and the quantum efficiency (φ). The absorption cross-section is related to the fluorescent molecules number density (N_T), the molar extinction coefficient (ε_F) and the molar concentration (C) through $\sigma = \varepsilon_F C / N_T$. The decay of

* fleblond@art.ca

Multimodal Biomedical Imaging II, edited by Fred S. Azar
Proc. of SPIE Vol. 6431, 643106, (2007) · 1605-7422/07/$18 · doi: 10.1117/12.700841

the fluorescence intensity is characterized by the sum of radiative and non-radiative decay rates (τ_r^{-1} and τ_{nr}^{-1}). Finally, the quantum efficiency, $\varphi = \tau_{nr}(\tau_{nr}^{-1} + \tau_r^{-1})$, is a measure of the number of photons emitted to the number of photons absorbed. The ideal situation for fluorescence imaging is when non-radiative contributions are absent ($\varphi = 1$). In the presence of a photon fluence source term $\Phi(r, t)$, which locally excites fluorophores, the typical *single exponential decay* is modified according to the time-dependent relation (see, *e.g.*, [6])

$$\frac{\partial N(\vec{r},t)}{\partial t} = -\frac{N(\vec{r},t)}{\tau} + \varphi\sigma\,\Phi(\vec{r},t)\left[N_T(\vec{r}) - 2N(\vec{r},t)\right] \quad (1)$$

where N represents the number density of excited fluorophores. In the limit where the quantum system of interest is non-saturated, *i.e.*, the number of excited molecules is much less than the total number of fluorophores ($N \ll N_T$), the frequency domain solution to (1) is

$$S(\vec{r},\omega) = \frac{N(\vec{r},\omega)}{\tau} = \frac{\varphi\varepsilon_F C(\vec{r})}{1 - i\omega\tau}\Phi(\vec{r},\omega)$$

where S is a fluorescence source term representing the Fourier transform of a photon density per unit time.

2.1. Photon transport in small animals

The physical process we wish to model consists in the injection of a collimated and coherent finite duration beam of NIR light into a biological tissue followed by photon detection at another spatial location. Typically, when propagating in biological tissues, photons are highly scattered. In terms of physical parameters this can be represented by a large ratio of the scattering over the absorption coefficient. This leads to rapid photons randomization after they have entered the medium implying, *e.g.*, that an incident laser pulse can be modeled as an isotropic source inserted some distance under the tissue surface. In order to correctly model light transport for arbitrary samples (optical parameters, shape, size), solutions to the full radiative transport theory should be considered [2]. The complexity of the associated integro-differential equation is such that the amount of CPU time required in order to solve it is prohibitive for the development of commercial tomography algorithms (however, see [3]). As a result, it is common in the field of diffuse optical imaging to consider the diffusion approximation (**DA**) [2, 4] to the radiative transfer equation. The resulting equation is the so-called time-dependent diffusion equation (**DE**),

$$\frac{n}{c}\frac{\partial\Phi(\vec{r},t)}{\partial t} - \vec{\nabla}\cdot D(\vec{r})\vec{\nabla}\Phi(\vec{r},t) + \mu_a(\vec{r})\Phi(\vec{r},t) = S(\vec{r},t) \quad (2)$$

where Φ is the photon fluence, μ_a the absorption coefficient, μ_s' the reduced scattering coefficient, n the index of refraction, c the vacuum speed of light and S a source term. Strictly speaking, this equation can be used only if the following conditions are satisfied: (1) the source-collection point distance is large enough for full photon randomization to have occurred, (2) the reduced scattering to absorption ratio is large, (3) the index of refraction is constant throughout the medium, (4) there are no non-scattering regions inside the medium.

Among the difficulties associated with small animal imaging is the uncertain validity of the DA for the relatively small volumes considered. While there exist methods for dealing with domains having different indices of refraction as well as with the presence of void regions (see, *e.g.*, [8, 9]), their application requires *a priori* knowledge. This information is certainly not available for the mono-modal imaging prototype considered in this document. Moreover, the high variability of optical properties due to organs and tissues [5, 7] makes it difficult to appreciate whether or not the DA is valid for all line-of-sights traced across the animal. In Section 2.3, we propose two distinct schemes, one of which relies on time-resolved technology, helping to minimize the impact of those heterogeneities in the scope of our fluorescence diffuse optical tomography (**FDOT**) algorithm. For the experimental setup under consideration (see Section 4 for details), light collection is performed across the animal (trans-illumination) allowing us to make the assumption that photon path lengths are always larger than what is required for the DA to hold.

2.2. Impact of boundary conditions

In the context of a tomography algorithm, solutions to (2) must be evaluated several times per image reconstruction, which imposes efficiency constraints on the resolution method used in commercial software. In this section, we propose a method adapted to rodent imaging and present some numerical results related to the inaccuracies introduced when using incorrect boundary conditions.

The curved nature of small animal surfaces complicates the modeling process. As mentioned in Section 4, our fluorescence imager prototype is equipped with a profilometer module providing a three-dimensional (**3D**) contour of the animal [1]. This means that for all source-detector pairs considered, the spatial location of photons' entering and exiting points are known within the accuracy of the profile and the focusing properties of the free beam optics. The profile information can also be used to estimate the local curvature of the animal surface. An aspect that must be treated mathematically is the index of refraction mismatch at the *air-tissue* and *glass-tissue* interfaces. The exact radiative transfer theory boundary condition at an interface $\partial\Omega$ requires the irradiance entering the medium from the outside to vanish [2]. In terms of the DA fluence, this takes the form of a Robin boundary condition,

$$\Phi(\vec{r},t) - 2AD\,\hat{s}\cdot\nabla\Phi(\vec{r},t) = 0 \quad \text{for} \quad \vec{r}\in\partial\Omega \quad (3)$$

where A depends on the reflection coefficient on $\partial\Omega$ as well as the local curvature of the sample [10, 15], and $\hat{s}$ is a normal unit vector. Finding analytical solutions to the DE satisfying mixed boundary conditions can be complicated. Reference [10] proposes a simple approximate scheme whereas the problem becomes Dirichlet by introducing the so-called linearly extrapolated boundary condition. Henceforth we adopt the latter, which postulates that the fluence identically vanishes a normal distance $d_e = 2AD$ away from the boundary.

Assuming the source term to be point-like in both spatial and temporal directions (for simplicity, the pulse originates from $r=0$ and $t=0$), the solution to (2) in the absence of an index mismatch is

$$\Phi_\infty(\vec{r},t) = \frac{N_0 c}{\left(\frac{4\pi Dc}{n}\right)^{3/2} n\,t^{3/2}} \exp\left(-\frac{n r^2}{4Dct} - \frac{\mu_a ct}{n}\right) \quad (4)$$

where N_0 is the total number of photons injected into the sample. Expression Φ_∞ is the basic object used for constructing DE solutions for more complex geometries having non-zero index mismatch. In fact, by using the method of image [11] one can obtain solutions to the DE for simple convex geometries such as the semi-infinite half-space, the infinite slab [12, 15], the parallelepiped [16] as well as the cylinder and the sphere [12]. These particular solutions are not adapted for mouse imaging where the surface curvature and the inter-scan tissue depths should not be neglected.

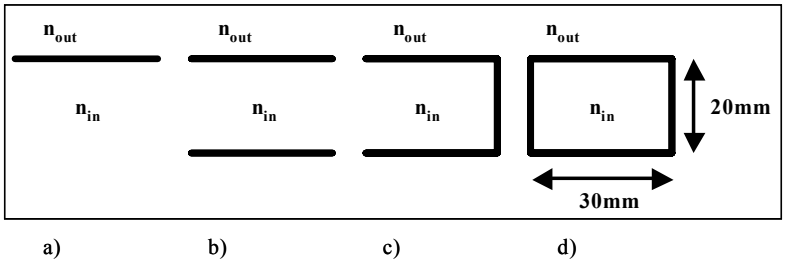

Figure 1: Geometries considered when analyzing the impact of mouse-like boundary conditions on the forward model associated with the FDOT algorithm: a) infinite half space, b) infinite slab, c) semi-infinite slab, d) slab. The direction going through the page is taken to be infinite.

A method for solving the DE inside a domain surrounded by an arbitrary boundary is the so-called Kirchhoff approximation [13, 14]. We have developed a somewhat related fast and generic numerical algorithm for computing approximate DE solutions inside a convex boundary composed of a finite number (N_p) of two-dimensional planes. Mainly, the algorithm input consists of the mathematical objects defining the N_p planes (*i.e.*, a 3D point lying on the plane and the components of a normal unit vector) as well as the index of refraction outside each plane. Then, for a given isotropic source location (usually inserted one mean free path length under the surface) and a collection point, the corresponding solution to the DE is calculated by considering the contribution of all relevant source images obtained by multiple reflections across the extrapolated planes. The iterative reflection process is stopped after convergence is reached according to a preset tolerance factor. In other words, the stopping criterion is reached when the addition of new image sources no longer contributes significantly to the solution.

As an application of our algorithm we present a preliminary analysis showing the impact of boundary conditions and varying optical properties on the following characteristics of a temporal point-spread function (**TPSF**): integrated intensity (I), mean photon arrival time (τ) and variance (σ). We consider four geometries composed of different

numbers of planes: the *infinite half space* (Figure 1a) with one plane separating two homogenous media having different indices of refraction; the *infinite slab* (Figure 1b) having two parallel planes with 20mm separation; the *semi-infinite slab* (Figure 1c) where an extra transverse plane is added, and finally, the *slab* (Figure 1d) with 30mm lateral size. For all these geometries we assume the dimension going through the page to be infinite. The geometry represented in Figure 1d has physical dimensions giving it some relevance for mouse imaging applications.

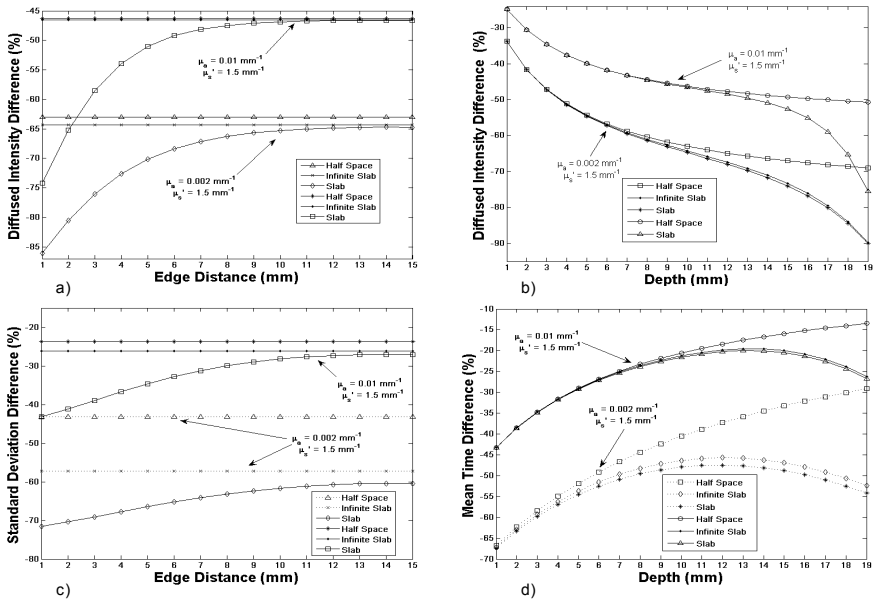

Figure 2: Graphs illustrating the impact of boundary conditions on the amplitude and shape of a TPSF: a) intensity as a function of distance from the edge of the sample, b) intensity as a function of detection point depth, c) standard deviation as a function of distance from the side edge of the sample, d) mean photon arrival time as a function of detection depth. For graphs a) and d) the detection point is at a 10mm depth. Graphs c) and d) are for source and collection points located 15mm away from both lateral walls of the slab.

Figure 2 illustrates the salient features of our analysis considering simple right-angled boundaries. The *y*-axis of our graphs shows the relative difference with respect to the no-boundaries solution (4). Graphs b) and d) consider an isotropic source inserted in the middle of the top boundary (x=15mm). The *x*-axis shows increasing depth values (with same *x*-*y* location as the source) for the evaluation of the DE solution. We find, as expected, that the corrections due to images sources are getting more important as the measurement point gets closer to the bottom boundary. For small values of the absorption the latter boundary becomes relevant for smaller depths because larger μ_a-values (and smaller scattering) tend to attenuate the diffusive effect (*e.g.*, the mean time and the variance are getting smaller). The error committed when neglecting the bottom boundary can be more than 10% for intensity and 20% for meantime when μ_a=0.01mm^{-1} and μ_s'=1.5mm^{-1}. Conclusions similar to those reached for the mean time are obtained for the TPSF standard deviation. For those cases where the source and detection points are located 15mm away from the lateral boundaries, we find the boundary effect to be small although the results are clearly more sensitive for small values of absorption and large values of scattering. To that effect, graphs a) and c) show the impact of taking the source and detection point (depth fixed at 10mm) closer to the rightmost slab boundary. Comparing results for the *infinite slab* with those for the *slab* we find discrepancies are increasing as the source and detectors approach the side boundary. In fact, errors committed when ignoring the lateral boundary can get as large as 10% for intensity and 30% for standard deviation. Similar results are obtained for the mean photon arrival time.

What happens physically is that because of the diffusive/non-diffusive interface, the pool of photons available for detection (integrated TPSF intensity) at a given point is reduced with respect to cases where there is no boundary. This is a direct consequence of the radiative transfer theory boundary condition mentioned at the beginning of this section. We have also observed that both mean time and variance are reduced in the presence of boundaries with respect to solution (4). This is explained by the fact that a TPSF associated with non-trivial surrounding geometry naturally excludes far-reaching photons absorbed by the boundaries that could otherwise be detected. As shown above this gives the illusion that diffusive effects are minimized.

2.3. Fluorescence diffuse optical forward model

The model expression for the TPSF collected at the detector is given by the convolution of three functions: (1) the propagator from the isotropic source to a fluorescent molecule inside the medium, (2) the quantum mechanical excitation and de-excitation of the fluorophore, and (3) the photon transport to the collection point. The Fourier components of this expression, including potential contributions from all infinitesimal volume elements, are (see, *e.g.*, [20])

$$\Phi^E(\vec{r}_d,\omega) = \frac{N_0}{\sqrt{2\pi}} \int d^3 r_f \;\; \Theta_d(\vec{r})\, G^E(\vec{r},\vec{r}_f,\omega) \frac{\varphi\, \varepsilon\, C_T(\vec{r}_f)}{1-i\omega\tau} \Theta_s(\vec{r}_s) G^X(\vec{r}_f,\vec{r}_s,\omega) \quad (5)$$

where the labels *s*, *d*, *f* respectively stand for *source*, *detection* and *fluorophore* locations while G^E and G^X represent the frequency domain Green functions of the diffusion equation (2) at the fluorophore emission and excitation wavelengths (λ^E and λ^X). In (5) we have included the source and detector experimental coupling constants Θ_d and Θ_s [21, 22]. Those parameters are essential because they contain, in principle, all information related to inconsistencies with the model due to systematic experimental errors. For example, these would include optical effects caused by defects on the surface of the animal that could not be accounted for in the scope of our diffuse optical model. In reality, the coupling factors cannot be determined directly for all source and detector pairs involved in a tomography algorithm. Therefore we consider the normalized field [21, 22]

$$\Phi^N(\vec{r},\omega) = \frac{1}{\sqrt{2\pi}} \frac{\Phi^E(\vec{r},\omega)}{\Phi^X(\vec{r},\omega)} \quad (6)$$

where Φ^X is the fluence collected at the fluorophore excitation wavelength. Experimentally, this field must be acquired separately from fluorescence data. Since the spatial locations of the source and detectors for both scans are identical, it can readily be seen that the coupling factors are cancelled in Φ^N. Roughly, the latter may be regarded as the Fourier components of the time-dependent fluorescent field from which *diffusive effects* have been removed. Of course this is not an exact statement because the paths (on average) followed by photons associated with the scans Φ^E and Φ^X are only approximately the same. However, it is believed that using the calibration scheme (6) can significantly reduce the impact of optical properties heterogeneities when homogeneous propagators are used [23]. Finally, it may be shown that the forward model expressions for the TPSF (integrated intensity, mean time and variance) for the normalized field are

$$\frac{\tilde{I}^E}{\tilde{I}^X} = \frac{N_0\, \varepsilon\, \varphi}{N_0^X} \int d^3 r_f \; C_T(\vec{r}_f) \; \frac{I_{df}^E \times I_{fs}^X}{I_{ds}^X} \quad (7)$$

$$\frac{\tilde{I}^E}{\tilde{I}^X}\left(\left\langle \tilde{t} \right\rangle^E - \left\langle \tilde{t} \right\rangle^X \right) = \frac{N_0 \varepsilon \varphi}{N_0^X} \int d^3 r_f C_T(\vec{r}_f) \frac{I_{df}^E \times I_{fs}^X}{I_{ds}^X} \left(\tau + \left\langle t \right\rangle_{df}^E + \left\langle t \right\rangle_{fs}^X - \left\langle t \right\rangle_{ds}^X \right) \quad (8)$$

$$\frac{\tilde{I}^E}{\tilde{I}^X}\left(\tilde{\sigma}^E - \tilde{\sigma}^X + \left[\left\langle \tilde{t} \right\rangle^E - \left\langle \tilde{t} \right\rangle^X \right]^2 \right) =$$

$$\frac{N_0 \varepsilon \varphi}{N_0^X} \int d^3 r_f C_T(\vec{r}_f) \frac{I_{df}^E \times I_{fs}^X}{I_{ds}^X} \left(\tau^2 + \sigma_{df}^E + \sigma_{fs}^X - \sigma_{sd}^X + \left[\left(\tau + \left\langle t \right\rangle_{df}^E + \left\langle t \right\rangle_{fs}^X - \left\langle t \right\rangle_{ds}^X \right) \right]^2 \right) \quad (9)$$

where tilted quantities correspond to properties evaluated directly from experimental data. Our notation is that I, $\langle t \rangle$ and σ respectively correspond to the integrated intensity, the mean time and the variance associated with a diffusion equation solution between two points [35], *i.e.*,

$$I = \sqrt{2\pi}\Phi(\vec{r},\omega)\Big|_{\omega=0}, \qquad < t >= (-i)\frac{\left.\frac{\partial \Phi(\vec{r},\omega)}{\partial \omega}\right|_{\omega=0}}{\Phi(\vec{r},\omega)\big|_{\omega=0}}, \; \sigma = -\frac{\left.\frac{\partial^2 \Phi(\vec{r},\omega)}{\partial \omega^2}\right|_{\omega=0}}{\Phi(\vec{r},\omega)\big|_{\omega=0}} - < t >^2 .$$

Equations (7)- (9) illustrate that the calibration technique based on an acquisition at the excitation wavelength can in fact be interpreted as a de-convolution of the signal associated with photons having propagated between the source and the detector at λ^X. Similarly, the contribution of the IRF (I_{IRF}, $\langle t \rangle_{IRF}$, σ_{IRF}) to the experimental signal can be directly

removed from the left-hand-side (**LHS**) in (7)- (9) [35]. The corresponding forward model expression for the skew of the TPSF has been computed but is not considered here for simplicity. We note that the derived forward model expressions are general in the sense that the mathematical entities I, $\langle t \rangle$ and σ are not necessarily computed using homogeneous Green functions. For example, they could be calculated with the generalized method of images presented in Section 2.2 and, also, with the full Newman series [17] taking into consideration the presence of μ_a and μ_s' heterogeneities for cases where *a priori* anatomical and structural information is available. However, it should be said that clear limitations associated with the perturbation theory approach were pointed out in [19]. A recent proposal for circumventing these limitations using radiative transport theory may be found in [18].

Finally, we note that a clear modeling advantage of having time-resolved data at our disposal is the possibility of estimating the mouse optical properties by diffusion curve fitting [36, 37] (see also [38]) with TPSF's collected at λ^X. In the scope of the FDOT algorithm, this task is performed for all source and detector pairs therefore reducing further the impact of optical properties heterogeneities present in small animals.

2.4. Inverse problem resolution method

In order to make the volume integrals in (7)-(9) numerically accessible, we consider a simple decomposition of the volume targeted for reconstruction into N_v square voxels. Then, each of the forward model equations becomes a finite sum over contributions from all voxels potentially contributing to the signal on the LHS. Considering TPSF's for N_s source locations associated with N_d collection points, the equations are concatenated into a matrix model of the form

$$\begin{bmatrix} b_I \\ b_{\langle t \rangle} \\ b_\sigma \end{bmatrix} = \begin{bmatrix} A_I \\ A_{\langle t \rangle} \\ A_\sigma \end{bmatrix} \left[C_T \right] \quad (10)$$

where the column vectors b_i ($i=\{I, \langle t \rangle, \sigma\}$) contain data calibrated as in (7)- (9).

Typically, the matrix A in (10) is semi-positive, rectangular, large and sparse. The process by which solutions to (10) are found is a particular instance of a bound-constrained linear least-squares problem. The classical linear least-squares problem (without constraints on the variables) has been studied extensively, and well-understood algorithms exist for the fast and robust solution of even large-scale problems (see, *e.g.*, [25]). However, the presence of constraints on the optimization variables considerably complicates the solution process.

A key goal of active-set algorithms for bound-constrained problems is to determine which variables have bounds that are *active* at the solution. These algorithms update an estimate of the optimal active set at each iteration. In effect, once the correct active set has been identified, the overall problem reduces to the classical (unconstrained) least-squares problem on the remaining variables. Most active-set algorithms are limited by the number of active-set changes that can be made at each iteration (usually, at each iteration this set can expand or contract by only a single index) or they are limited by the effectiveness of the linear algebra technology used to update the matrix factorization that underlies the algorithm. Algorithms based on these approaches typically have difficulty scaling to large problems (a review of active-set approaches may be found in [25] and [30]). We also note that significant, and more recent, alternatives to the active-set approaches described above are interior-point methods (see [26] and [29] for reviews). Such algorithms have been shown to scale well for large problems. However, for such algorithms it is not known how to effectively take advantage of good starting points (*i.e.*, good estimates of the solution), or how to employ iterative linear-algebra techniques that are best suited for problems where the data is only known implicitly (*e.g.*, the matrices are only available as operators).

The BCLS algorithm that we describe in this section belongs to the class of active-set methods, but tries to overcome some of the typical deficiencies of this class by employing techniques that make large changes to the active-set at each iteration, and yet continues to be amenable to linear-algebra techniques that scale well with the problem size. We describe the BCLS algorithm in the context of the generic least-squares problem

$$\underset{x \in \mathrm{R}^n \text{ s.t. } l \le x \le u}{\text{minimize}} \quad \frac{1}{2}\left\| Ax - b \right\|_2^2 + c^T x + \frac{1}{2}\gamma^2 \left\| x \right\|_2^2 \quad (11)$$

where x is the vector of optimization variables, A is an m x n coefficient matrix, and b and c are respectively m- and n-vectors. The n-vectors l and u are lower and upper bounds on the optimization variables. The regularization parameter γ can be used to control the norm of the final solution.

The BCLS algorithm is based on a two-metric projection method [24] for which a partitioning of the variables is maintained at all times. Variables that are well within the interior of the feasible region are labeled *free,* while variables that are at (or near) one of the bounds are labeled *fixed*. Conceptually, x, A and c are partitioned into their free (B) and fixed (N) components:

$$x = (x_B, x_N), \qquad c = (c_B, c_N), \qquad A = [A_B \;\; A_N].$$

At each iteration, the two-metric projection method generates independent descent directions Δx_B and Δx_N for the free and fixed components of x; these are generated from an approximate solution to the block-diagonal linear system

$$\begin{bmatrix} A_B^T A_B + \gamma^2 I & 0 \\ 0 & D \end{bmatrix} \begin{bmatrix} \Delta x_B \\ \Delta x_N \end{bmatrix} = A^T r - c - \gamma^2 x \quad (12)$$

where $r=b-Ax$ is the current residual, D is a diagonal matrix with strictly positive entries, and the right-hand side is the negative of the gradient (Jacobian) of (11). Hence, a Newton step is generated for the free variables and a scaled steepest-descent step is generated for the fixed variables. The aggregate step (Δx_B, Δx_N) is then projected into the feasible region and the first minimizer is computed along the piecewise linear projected-search direction [27].

The linear system (12) is never formed explicitly. Instead, Δx_B is computed equivalently as a solution to the least-squares problem

$$\underset{\Delta x_B}{\text{minimize}} \quad \frac{1}{2}\left\| A_B \Delta x_B - r \right\|_2^2 + c_B^T \Delta x_B + \frac{1}{2}\gamma^2 \left\| x_B + \Delta x_B \right\|_2^2 \quad (13)$$

We find an approximate solution to (13) by applying the conjugate-gradient-type solver LSQR [32] to the problem

$$\underset{\Delta x_B}{\text{minimize}} \left\| \begin{bmatrix} A_B \\ \beta I \end{bmatrix} \Delta x_B - \begin{bmatrix} r \\ \frac{1}{\beta} c_B - \frac{\gamma^2}{\beta} x_B \end{bmatrix} \right\|_2 \quad (14)$$

where $\beta = \max\{\gamma, \varepsilon\}$ with ε a small positive constant. If $\gamma < \varepsilon$, the resulting step is effectively a modified Newton step. Although this can lead to slower convergence, it has the advantage of safeguarding against rank-deficiency in the current sub-matrix A_B. In order to control the amount of work carried out by LSQR in the solution of the least-squares sub-problems (14), BCLS employs an inexact Newton strategy in order to control the accuracy of the computed sub-problem solutions Δx_B [28]. This approach can significantly reduce the amount of work required by the algorithm, which is determined by the total number of matrix-vector products with matrices A_B and its transpose.

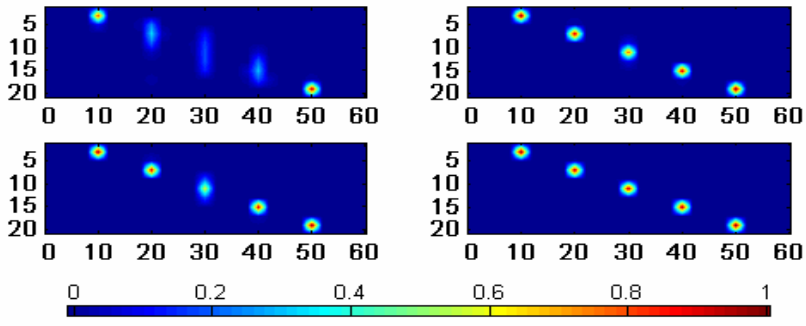

Figure 3: Reconstructed images using four 9-detectors configurations: single line with 3mm interspacing, 24mm FOV (bottom-right corner), square array with 6mm interspacing, 12mm FOV (top-right corner), square array with 3mm interspacing, 6mm FOV (top-left corner), cross with 3mm interspacing, 12mm FOV (bottom-left corner).

3. SIMULATIONS

To test the robustness of the inverse problem resolution technique presented in Section 2.4, we have performed numerous simulations based on synthetic data vectors generated using the forward model described in Section 2.3. Our aim is to determine the impact on reconstruction quality of certain parameters such as the noise level, data type combinations and detector arrangement. We consider a synthetic phantom composed of five $8mm^3$ cubic fluorophore inclusions with 10mm spatial separation in the *x*-*y* plane and various center-of-mass depths (3mm, 7mm, 11mm, 15mm, 19mm). The inclusions are made to model a substance containing 1nM concentration of Cy5.5 fluorescent molecules. The maximum of the absorption spectrum for this molecule is at 675nm with molar extinction coefficient ε=2.5x10^{-5}M^{-1}mm^{-1}, quantum efficiency φ=0.23 and lifetime τ=1.0ns. The emission fluorescence maximum for Cy5.5 is at 694nm. The medium into which the inclusions are embedded is a 22mm thick infinite slab with optical properties μ_a=0.03mm^{-1} and μ_s'=1.0mm^{-1}. For simplicity, we assume the optical properties spectra to be flat. The index of refraction for the diffusing medium is n=1.4 as is commonly used for animal tissues [40] while the exterior medium is considered to be air (n=1). Using data vectors associated with the phantom described above, the least-squares problem (11) is solved after preconditioning the matrix similarly as in [31]. In order to test the noise stability of the procedure we simply added a normally distributed contribution with zero mean to all members of a given data type set. The corresponding Gaussian noise standard deviation is calculated as a fixed percentage of the numerical value associated with the data. Henceforth all images shown (including Section 4) are *x*-*z* planes intersecting the inclusions at their center along the *y*-axis.

The first aspect we consider is the impact on image quality of varying the relative positioning of the detectors. A study to that effect is performed in [33, 34] where a detector placement optimization is considered based on a singular value analysis of the *continuous wave* forward model matrix. Unfortunately, the results of [33, 34] as well as the technique utilized cannot be applied to our problem of interest because the bound-constrained feature of the least-squares algorithm implies that the building blocks of the solutions are not necessarily the lower frequency right singular vectors of the full forward matrix A (or its generalized GSVD representation). As described in Section 2.4, when the non-negative constraint is activated the BCLS algorithm repetitively solves related but different LSQR problems until a minimum least-squares solution is reached. This implies that solutions at different iterations are built out of vectors from a Krylov subspace computed based on (13) rather than (11). We therefore embarked on performing a more *ad hoc* experimental optimization based on maximizing the tissue sampling and the number of projections [39]. The subset of configurations considered in this note is composed of the following four arrangements of 9 detectors: single line with 24mm field-of-view (**FOV**), square array with 12mm FOV, square array with 6mm FOV, and cross with 12mm FOV. As illustrated in Figure 3, our preliminary analysis shows that increasing the detector FOV is synonymous with increasing image quality. Secondly, we consider the impact of using different data type combinations on the quality of the fluorescence images. Figure 4 illustrates our results (10% noise added) in the case of four combinations: intensity alone, mean time alone, intensity plus mean time, and all three data types. Based on the simple phantom considered here we find that adding more data types is beneficial and leads to better localization and contrast recovery for inclusions located deep into the medium. Finally, we evaluated the impact of reconstructing from data with different noise levels. Figure 5 shows fluorescence images reconstructed with all three data types for noise levels varying from 0% to 10%. In the absence of noise, all five inclusions are perfectly reconstructed (full maximum amplitude recovery, negligible center-of-mass error and spreading along all three axes). As noise is added it becomes increasingly difficult to localize deep inclusions. In general, we find BCLS to be quite robust to noise. In fact for the 1% and 5% noise images all inclusions can be precisely located. For the 1%, case contrast recovery remains very close to the expected value.

For the studies presented in this section the penalty terms in (11) were set to zero. This means the only regularization used is intrinsic (*i.e.*, conjugate-gradient type [41]). For all cases considered, a non-negative constraint was imposed, which significantly reduces the size of the solution space. We found that whenever the non-negative constraint is relaxed, the quality of the reconstructed images is largely degraded. We have also investigated the impact of using Tikhonov regularization by plotting *L*-curves for some combinations of data types and different noise levels. Typically, we find that the optimal solution (*i.e.*, the one at the corner of the *L*-curve) is always smeared leading to images that are much more blurred than the results shown in this section.

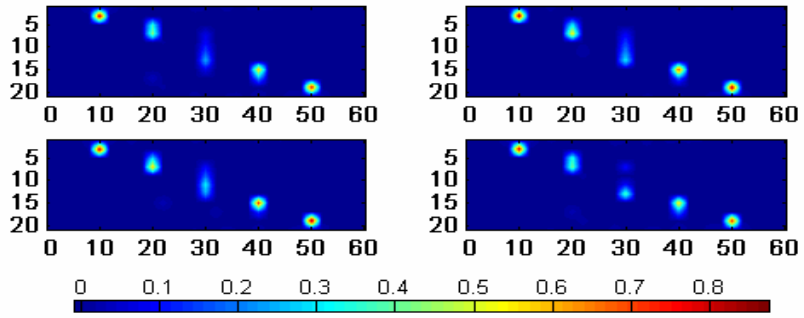

Figure 4: Reconstructed images using different data type combinations: integrated intensity (top-left corner), intensity and mean time (top-right corner), mean time (bottom-right corner), intensity, mean time and variance (bottom-left corner).

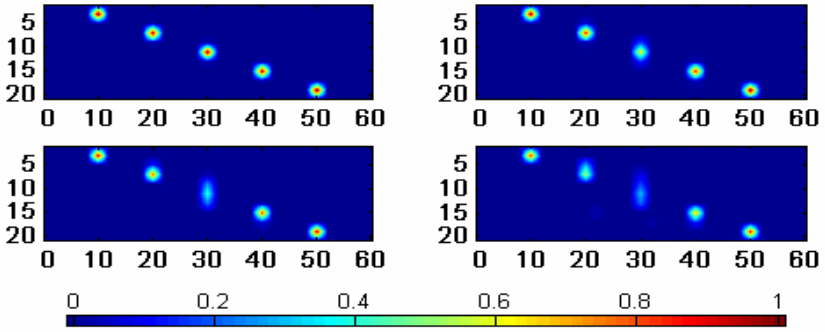

Figure 5: Reconstructed images for different levels of data noise: 0% (top-left corner), 1% (top-right corner), 5% (bottom-left corner), and 10% (bottom-right corner).

4. EXPERIMENTAL RESULTS

Measurements were performed with a time-resolved prototype using an 80MHz repetition rate pulsed laser diode (PicoQuant, Berlin, Germany) with 150 picoseconds (**ps**) maximum pulse duration and 670nm central wavelength. The scanning system configuration is built in transmission. The detection system is composed of a time-correlated single photon counting (**TCSPC**) module (Becker & Hickl, Berlin, Germany) coupled to a Hamamatsu Photonics (Hamamatsu City, Japan) photomultiplier tube (**PMT**) with an approximate 350ps time response and spectral sensitivity in the 380 to 890nm range. The collection point is raster-scanned over the sample using galvanometric mirrors in a telecentric free-beam optical design. The collimated source is coupled to a filter (Omega Optical, Brattleboro, Vermont) and delivers light to an optical fiber and then to an attenuator module (OZ Optics, Ottawa, Ontario). The laser beam is delivered to a folding mirror re-directing light at the specimen from beneath, across a polycarbonate plate (index of refraction n=1.49). The folding mirror is mounted onto a manual linear x-y translational stage (ThorLabs, Newton, New Jersey) allowing scans to be performed with as much as 0.01mm precision. For imaging with Cy5.5 (Amersham Biosciences, Buckinghamshire, England), the fluorescence signal is submitted to a 700nm long-pass filter prior to entering the PMT. A 670nm band-pass filter (20nm width) may also be used for signal acquisition. The system is also equipped with a charge-coupled device (**CCD**) camera combined with a 675nm laser to reconstruct a three-dimensional profile of the sample with <1mm precision. The finite time response of the system has approximate 300ps width.

In this section we present a preliminary experimental performance evaluation of the FDOT algorithm. We consider a rectangular phantom built out of polyurethane with a certain concentration of scattering agent added, *i.e.*, a powder composed of 1-2μm titanium dioxide (TiO_2) particles. The resulting optical properties at λ=670nm were found to be approximately μ_a=0.002mm^{-1} and μ_s'=1.0mm^{-1}. The index of refraction of the polyurethane was measured using an optical matching liquid technique and found to be n=1.5. The thickness of the sample is 20mm while the lateral dimensions are 100mm and 40mm. Three cylindrical inclusions (2mm height, 2.5mm radius) with specific Cy5.5 concentrations were embedded in the matrix in order to simulate fluorescent regions inside a biological tissue. Inclusion concentrations and center-of-mass depths (from left to right in Figure 6) are: (3mm, 100nM), (3mm, 50nM) and (6mm, 50nM). The *x*-*y* center-of-mass difference between successive inclusions is 30mm. Illumination of the sample is performed with a 2mm resolution along both the *x*- and *y*-axes for a grid composed of 38 by 8 scan points. For each scan point, a centered grid made out of 5 by 5 collection points with 3mm interspacing along both axis is used. In total, this corresponds to 7600 source-detector pairs available for reconstruction purposes. The laser power used for the fluorescence scan is ~1mW (1s integration time for each point) while that for the scan performed at the excitation wavelength is ~14μW (0.1s integration time). As an indication of noise level during the experiment, the most intense signal acquired in fluorescence had a TPSF peak of 2150 photons.

Figure 6 shows a reconstructed image of the experimental phantom with data normalized using a scan with acquisition at the excitation wavelength. It is worth noting that no image normalization was used and that the maximum recovered amplitude (in nM) is within 12% of the expected value and the center-of-masses are within 1mm. For the case shown on the figure, integrated intensity and mean photon time arrival were used. The reconstruction was performed using the same inverse problem setup (pre-conditioning, scaling) as in Section 3. The lifetime value used in the forward model is 1.8ns as found using the single lifetime fitting feature of the OptiView™ software distributed by ART with the Explore Optix™ system.

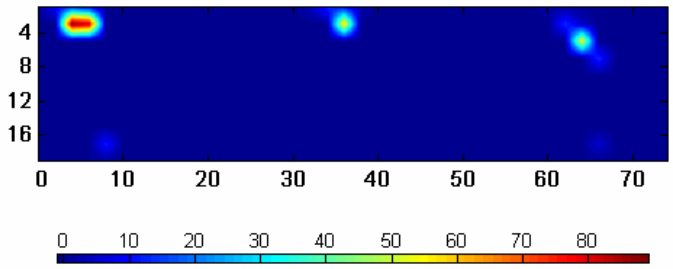

Figure 6: Reconstruction using experimental data normalized with a scan performed at the excitation wavelength (5 detectors arranged in a line with 3mm spacing). Image shown is obtained with both integrated intensity and mean time.

5. CONCLUSION

We have presented an algorithm based on time-resolved data for reconstructing 3D images of fluorescence emanating from the interior of a small animal. A forward model based on TPSF moments was presented emphasizing the impact of boundaries between diffusive and non-diffusive media. We have shown that, due to the small size of the animals, boundary effects are enhanced which implies they cannot be neglected. In particular, the shape of a time-dependent diffusion curve acquired close to the edge of an animal is expected to be significantly different from one acquired closer to its geometrical center. This implies that ignoring the animal profile will not only lead to forward model errors, but can also induce important optical properties errors during the fitting process (Section 2.3) further compromising fluorescence image quality. Finally, we have presented preliminary optimization analysis for the FDOT algorithm in terms of data type combinations and detector arrangements. More details and further analysis (*e.g.*, impact of optical properties heterogeneities and background fluorescence) will be presented elsewhere.

ACKNOWLEDGEMENTS

We would like to express our gratitude to Muriel Jean-Jacques and Niculae Mincu at ART, as well as to Brian Pogue and Subha Srinivasan for useful comments and discussions.

REFERENCES

1. M. Takeda, K. Mutoh, "Fourier transform profilometry for the automatic measurement of 3-D object shapes," Appl. Opt. **24**, 3977-3982 (1983). **[9]**
2. A. Ishimaru, *Wave Propagation and Scattering in Random Media*, Academic Press, New York, 1978. [**2**]
3. A. D. Klose, U. Netz, J. Beuthan, A. H. Hielscher, "Optical tomography using the time-independent equation of radiative transfer – Part 1: forward model," J. of Quantitative Spectroscopy & Radiative Transfer **72**, 691-713 (2002). [**3**]
4. S. R. Arridge, "Optical Tomography in medical imaging," Inverse Problems **15**, R41-R93 (1999). [**4**]
5. G. Alexandrakis, F. R. Rannou, A. F. Chatziioannou, "Tomographic bioluminescence imaging by use of a combined optical-PET (OPET) system: a computer simulation feasibility study," Phys. Med. Biol. **50**, 4225-4241 (2005). [**7**]
6. A. Yariv, *Quantum Electronics*, John Wiley & Sons, New York, 1988. [**1**]
7. G. Alexandrakis, F. R. Rannou, A. F. Chatziioannou, "Effect of optical property estimation accuracy on tomographic bioluminescence imaging: simulation of a combined optical-PET (OPET) system," Phys. Med. Biol. **51**, 2045-2053 (2006). [**8**]
8. J. Ripoll, M. Nieto-Vesperinas, S. R. Arridge, H. Dehgani, "Boundary conditions for light propagation in diffusive media with nonscattering regions," J. Opt. Soc. Am. A **17**, 1671-1681 (2000). **[5]**
9. J. Riley, H. Dehghani, M. Schweiger, S. R. Arridge, J. Ripoll, M. Nieto-Vesperinas, "3D optical tomography in the presence of void regions," Optics Express **7**, 462-467 (2000). **[6]**
10. R. Aronson, "Boundary conditions for diffusion of light," J. Opt. Soc.Am. A 12, 2532-2539 (1995). [**10**]
11. J. D. Jackson, *Classical Electrodynamics*, John Wiley & Sons, New York, 1962. **[12]**
12. S. R. Arridge, M. Cope, D. T. Delpy, "The theoretical basis for the determination of optical pathlengths in tissue: temporal and frequency analysis," Phys. Med. Biol. **37**, 1531-1560 (1992). [**13**]
13. J. Ripoll, V. Ntziachristos, R. Carminati, M. Nieto-Vesperinas, "Kirchhoff approximation for diffusive waves," Phys. Rev. E **64**, 051917 1-8 (2001). [**15**]
14. J. Ripoll, V. Ntziachristos, "Iterative boundary method for diffuse optical tomography," J. Opt. Soc. Am. A **20**, 1103-1110 (2003). [**16**]
15. D. Contini, F. Martelli, G. Zaccanti, "Photon migration through a turbid slab described by a model based on diffusion approximation. I. Theory," Appl. Opt. **19**, 4587-4599 (1997). [**11**]
16. A. Kienle, "Light diffusion through a turbid parallelepiped," J. Opt. Soc. Am. A **22**, 1883-1888 (2005). [**14**]
17. M. R. Ostermeyer, S. L. Jacques, "Perturbation theory for diffuse light transport in complex biological tissues," J. Opt. Soc. Am. A **14**, 255-261 (1997). [**22**]
18. A. Sassaroli, F. Martelli, S. Fantini, "Perturbation theory for the diffusion equation by use of the moments of the generalized temporal point-spread function. I. Theory," J. Opt. Soc. Am. A **9**, 2105-2118 (2006). [**24**]
19. D. A. Boas, "A fundamental limitation of linearized algorithms for diffuse optical tomography," Optics Express **13**, 404-413 (1997). [**23**]
20. S. Lam, F. Lesage, X. Intes, "Time domain fluorescent diffuse optical tomography: analytical expressions," Optics Express 13, 2263-2275 (2005). [**17**]
21. V. Ntziachristos and R. Weissleder, "Experimental three-dimensional fluorescence reconstruction of diffuse media by use of a normalized Born approximation," Opt. Lett. **12**, 893-895 (2001). [**18**]
22. E. E. Graves, J. Ripoll, R. Weissleder, and V. Ntziachristos, "A submillimeter resolution fluorescence molecular imaging system for small animal imaging," Med. Phys. **30**, 901-911 (2003). [**19**]
23. A. Soubret, J. Ripoll, V. Ntziachristos, "Accuracy of fluorescent tomography in the presence of heterogeneities," IEEE Transactions on Medical Imaging **24**, 1377-1386 (2005). **[20]**
24. D. P. Bertsekas, *Constrained Optimization and Lagrange Multiplier Methods*, Academic Press, New York, 1982. **[32]**
25. A. Björk, *Numerical Methods for Least Squares Problems*, Society of Industrial and Applied Mathematics, Philadelphia, 1996. [**28**]

26. S. Boyd, L. Vandenberghe, *Convex Optimization*, Cambridge University Press, New York, 2004. [**30**]
27. A. R. Conn, N. I. M. Gould, P. L. Toint, *Trust-Region Methods*, MPS-SIAM Series on Optimization, Society of Industrial and Applied Mathematics, Philadelphia, 2000. [**33**]
28. R. S. Dembo, S. C. Eisenstat, T. Steihaug, "Inexact Newton Methods," SIAM J. Numer. Anal. **19**, 400-408 (1982).
29. A. Forsgren, P. E. Gill, M. H. Wright, "Interior methods for nonlinear optimization," SIAM Review **44**, 525-597 (2002).
30. C. L. Lawson, R. J. Hanson, *Solving Least Square Problems*, Society of Industrial and Applied Mathematics, Philadelphia, 1974.
31. O. E. Livne, G. H. Golub, "Scaling by binormalization," Numerical Algortihms **35**, 97-120 (2004).
32. C. C. Paige, M. A. Saunders, "LSQR: An algorithm for sparse linear equations and sparse least squares," ACM Trans. Math. Software **8**, 43-71 (1982).
33. J. P. Culver, V. Ntziachristos, M. J. Holboke, and A. G. Yodh, "Optimization of optode arrangements for diffuse optical tomography: A singular-value analysis," Opt. Lett. **26**, 701-703 (2001).
34. E. E. Graves, J. P. Culver, J. Ripoll, R. Weissleder, V. Ntziachristos, "Singular-value analysis and optimization of experimental parameters in fluorescence molecular tomography," J. Opt. Soc. Am. A 21, 231-241 (2004).
35. E. Hillman, "Experimental and theoretical investigations of near infrared tomographic imaging methods and clinical applications," PhD thesis (University College London, 2002).
36. M. S. Patterson, B. Chance, B. C. Wilson, "Time resolved reflectance and transmittance for the non-invasive measurement of tissue optical properties," Appl. Opt. **28**, 2331-2336 (1989).
37. V. Ntziachristos, B. Chance, "Accuracy limits in the determination of absolute optical properties using time-resolved NIR spectroscopy," Med. Phys. **28**, 1115-1124 (2001).
38. A. Liebert, H. Wabnitz, D. Grosenick, M. Moller, R. Macdonald, H. Rinneberg, "Evaluation of optical properties of highly scattering media by moments of distributions of times of flight of photons," Appl. Opt. **28**, 5785-5792 (2003).
39. B. W. Pogue, T. O. McBride, U. L. Osterberg, K. D. Paulsen, "Comparison of imaging geometries for diffuse optical tomography of tissue," Optics Express **4**, 270-286 (1999).
40. F. P Bolin, L. E. Preuss, R. C. Taylor and R. J. Ference, "Refractive index of some mammalian tissues using a fiber optic cladding method," Appl. Opt. **28**, 2297-2302 (1989).
41. P. C. Hansen, *Rank-Deficient and Discrete Ill-Posed Problems*, Society for Industrial and Applied Mathematics, Philadelphia, 1998.